Hindawi
Mathematical Problems in Engineering
Volume 2020, Article ID 7356740, 21 pages
https://doi.org/10.1155/2020/7356740

Research Article

Study on the Strata Movement Rule of the Ultrathick and Weak Cementation Overburden in Deep Mining by Similar Material Simulation: A Case Study in China

Guojian Zhang[1,2] **Guangli Guo**[2,3] **Yi'nan Lv**[4] **and Yaqiang Gong**[2]

[1]*NASG Key Laboratory of Land Environment and Disaster Monitoring, China University of Mining and Technology, Xuzhou 221116, China*
[2]*School of Environmental Science and Spatial Informatics, China University of Mining and Technology, Xuzhou 221116, China*
[3]*Jiangsu Key Laboratory of Resources and Environmental Information Engineering, China University of Mining and Technology, Xuzhou 221116, China*
[4]*School of Architecture & Design, China University of Mining and Technology, Xuzhou 221116, China*

Correspondence should be addressed to Guangli Guo; guo_gli@126.com and Yaqiang Gong; undergyq@cumt.edu.cn

Received 30 September 2019; Revised 7 March 2020; Accepted 13 March 2020; Published 25 April 2020

Academic Editor: Ali Ramazani

In the deep mining areas of western China, there exist ultrathick and weak cementation strata in the overburdens above the Jurassic coal seams, and the overburden lithology is generally moderately a little weaker than the medium-hard strata. Yet, the practical measurement indicates that the surface movement rule in this area displays the specialty that is apparently inconsistent with its lithology, which increases the uncertainty of safe production in coal mines. In this study, the similar material and numerical simulations were conducted to investigate the movement rule and failure pattern of the ultrathick and weak cementation overburden. In addition, the photographing scale transformation-time baseline parallax (PST-TBP) method was used to monitor the similar material model to makeup for the lacks of Xi'an Jiaotong University Digital Close-range Industrial Photogrammetry System (XJTUDP) software. The findings of this study can be summarized as follows. (1) To some extent, the PST-TBP method can makeup for the deficiency of the XJTUDP software because the measurement accuracy of the PST-TBP method is 0.47 mm. (2) The height of the caving zone is approximately 66 m, and the height of the water suture zone is about 112 m, which is obviously larger than that of the medium-hard and soft overburden in eastern-central China. (3) The first breaking span of the immediate roof reaches 120 m, the cyclic fracturing length is about 60 m, and the separation occurred at 43 m and 66 m above the coal seam. (4) The failure pattern of the ultrathick and weak cementation overburden is "beam-arch shell," and the failure boundary is arch. (5) The Zhidan group sandstone and Jurassic sandstone formations have strong control effects. The Zhidan group sandstone is the main control stratum and the Jurassic sandstone formation is the secondary-control stratum. The research results provide an insight into guiding the safe mining of deep coal in the ultrathick and weak cementation overburden.

1. Introduction

Western China is on its way to become the primary source of coal resources for China in the future. For example, the Ordos Basin (Inner Mongolia province) is one of the five major energy bases in China, and deep coal reserves in the Ordos Basin are much larger than those of shallow coal. This suggests that the exploitation of coal resources in the deep mining areas in the western region has important strategic significance for the energy development of this country. Because of large mining depths, there are ultrathick weak cementation strata in the overburden above the Jurassic coal seam [1, 2]. These strata are characterized by low strength, poor cementation, and easy weathering, and their lithology is generally exhibiting a little weaker than medium-hard stratum [3, 4]. However, the actual measurements find that the surface under full mining conditions performs the movement deformation features under the condition of

insufficient mining. It indicates that this phenomenon is obviously inconsistent with its lithology and quite different from the existing understanding. Thus, the stratum movement rule of deep mining with the ultrathick weak cementation overburden is complex and needs to be urgently resolved.

Currently, many studies focus on the rule of overburden movement caused by coal mining in eastern-central China. The rule of strata movement caused by the middle-shallow coal mining has been well studied by some researchers, such as Ju and Xu [5] who prosed the key stratum theory and Zuo et al. [6] who developed a "hyperform" model. In eastern China, the investigation of the overburden movement mechanism in deep coal mining has also resulted in growing research outputs. For example, Li et al. found that, under deep and insufficient mining conditions, the surface movement has characteristics of the absence of surface active period, delayed surface movement period, and no advanced impact angle, and the largest sinking lag angle was much smaller than that in shallow mining [7]. Xu et al. and Yu et al. employed the UDEC numerical simulation software to simulate the effects of key strata on the surface subsidence when the mining depth was 300 m and 800 m, respectively. It is difficult for deep mining to reach full mining due to the increased number of key strata in deep mining and the interaction between key strata. In the meantime, the increasing number of key strata can alter the movement rule of the stratum internal and enlarge the influence scope of deep mining [8, 9]. Wang et al. discovered that there was a sudden change in the surface movement of deep mining, and before this sudden change there was a bending-type sinking. After the sudden change point, there was fracture-type sinking. These findings break the concept that the relationship between the surface subsidence rate and the width-depth ratio shows continuous change and the corresponding curve passes through the origin [10]. Based on the observation data from deep multiple working faces mining of the Zhangxiaolou mining area in Xuzhou, Wang et al. found that the subsidence basin movement values caused by the deep multiworking faces mining were smaller than those caused by the shallow mining under the same mining degree conditions, and the cases of the discontinuous deformation reduce. The sinking rate, the sinking coefficient, and the mining depth show a natural logarithmic relationship [11].

Some scholars have conducted exploratory researches on the strata movement rule and prediction of deep mining area in western China. For example, Sun investigated the characteristics of the overburden movement in the weak cementation with a large mining thickness and concluded that the fracture zone evolution rule of the weak cementation overburden was consistent with the evolution rule of the caving zone [12]. Sun et al. deduced the development height of the water suture zone of the weak cementation overburden, offering data upkeep for the working face layout under such strata conditions [13]. Li et al. worked on the surface movement rule caused by the deep mineral resources mining under soft rock. From their work, it was found that the influence scope of deep mining expanded, and the growth rate of horizontal movement was faster than that of surface subsidence, and it reached a maximum subsidence value in a short time after mining [14]. Yang et al. [15] and Yu et al. [16] individually analyzed the surface measured data of Xiagou Coal Mine and Tingnan Coal Mine and established that the Luohe sandstone had strong deformation resisting capability, which can effectively control surface deformation. Due to the control of the Luohe sandstone, under the insufficient mining conditions, the surface movement is characterized by the surface movement rule under the extremely insufficient mining. Wang [17] and Lin [18] utilized the physical simulation and numerical simulation to investigate the strata movement rule under the condition of deep single working face mining in weak cementation overburdens and examined the causes of the small surface subsidence.

From the above research studies, it can be seen that the current scholars have performed plenty of studies on the mechanism of the overburden movement in the coal mining of eastern China and grasp it. However, in western China, the research on the deep mining area of ultrathick and weak cementation overburden is chiefly concentrated on the strata movement rule under the condition of extremely insufficient mining degree or insufficient mining degree. There is a lack of research on the stratum movement rule caused by large-scale mining deep coal resources under ultrathick weak cementation overburden.

Thus, this paper primarily applies physical simulation with the support of numerical simulation to deeply conduct the strata movement rule of deep multiple working faces mining of ultrathick and weak cementation overburden, revealing the movement mechanism of ultrathick and weak cementation overburden.

2. Geological Prototype

Dongsheng coalfield is located at the junction of Gaotouyao Community, Wushenqi Community, and Zhungeer-Linxian Community, with widely distributed sand dunes, sand ridges, and sandy land (Figure 1). Because of the special diagenetic environment, diagenetic age, and sedimentary process, a weak cementation overburden is formed with the characteristic of low strength, poor cementation, and easy weathering. The chief coal-bearing strata are the Jurassic Zhiluo formation and Yan'an formation, and their overlying strata are in order of the Cretaceous, Neogene, and Quaternary from bottom to top.

In addition, we collected a large amount of surface measured data from different coal mines in Dongsheng coalfield and obtained the surface subsidence coefficient of the corresponding mining area via inversion. For more information, see Table 1. The geological conditions for deep mining were collected in Yingpanhao Coal Mine, Bayan Gaole Coal Mine, and Nalinhe-2 Coal Mine, with Table 2 attained after the simplification.

It can be seen from Table 1 that the working face 2201 of Yingpanhao Coal Mine was mined, the surface subsidence was 309 mm, and the corresponding surface subsidence coefficient was 0.08. Besides, the working face 31101 of Nalinhe-2 Coal Mine was mined, with the surface

(a) (b)

Figure 1: Local geomorphological features of Dongsheng coalfield.

Table 1: Surface subsidence coefficient of some coal mines in Dongsheng coalfield.

Working face	Mining width (m)	Advancing width (m)	Mining height (m)	Mining depth (m)	Loose (m)	Bedrock ply (m)	q
Daliuta 12205	230	2251	3.50	110	22	88	0.73
Liuta 12106	246.8	633	6.90	151	30	120.6	0.77
Fengjiata 1201	250	1850	3.30	147	10	137	0.75
Cuncaota 22111	224	2085	2.80	249	8	240.9	0.68
Buertai 22103-1	360	4250	2.90	292	19	273	0.64
2-Cuncaota 22111	300	3648	2.90	305	15	294	0.68
Xiaojihan 11203	240	2245	2.67	350	25	315	0.60
Bayan Gaole 311101~311103	810	2600	5.30	650	118	532	0.44
Nalinhe-2 31101	240	3030	5.50	650	78	572	0.16
Yingpanhao 2201	300	1800	6.00	725	45	680	0.08

Table 2: Stratigraphic characteristics of some deep mining areas in Dongsheng coalfield.

Stratum			Yingpanhao	Bayan Gaole	Nalinhe-2
System		Formation	Thickness (m)		
Quaternary	Holocence		45.72–123.61 86.41	73.92–161.60 118.74	49.38–83.84 65.56
	Upper pleistocene	Malan formation			
Cretaceous	Zhidan group		253.04–429.91 347.77	104.46–255.88 178.67	53.88–279.08 138.31
Jurassic (chief coal-bearing strata)	Lower and middle Jurassic	Anding formation	50.9–134.80 94.66	35.90–157.29 96.60	67.53–154.53 103.15
		Zhiluo formation	126.26–229.34 169.72	71.12.00–238.60 154.86	111.92–199.34 151.44
		Yan'an formation	307.80–393.14 355.07	208.67–312.28 260.47	334.32–365.30 349.81

subsidence of 520 mm and the corresponding surface subsidence coefficient of 0.16. The working faces 311101, 311102, and 311103 were mined in Bayan Gaole Coal Mine. The surface subsidence was 2064 mm and the corresponding surface subsidence coefficient was 0.44. It can be found that, under the same mining degree, the surface subsidence coefficient in the deep mining area of Dongsheng coalfield was significantly smaller than that in eastern China. When the degree of mining was close to full mining, it still exhibits the characteristics of extremely inadequate mining. After analyzing the surface subsidence coefficient of the shallow and deep coal mines in Table 1, it far exceeded the difference in surface subsidence caused by a single factor, the mining depth, changing. Thus, we further analyzed the geological mining conditions in the deep mining area of Dongsheng coalfield. From the stratum structure of Yingpanhao Coal Mine, Nalinhe-2 Coal Mine and Bayan Gaole Coal Mine in Table 2, the single layer thickness of the weak cementation sandstone in the deep mining area of Dongsheng coalfield was large, without bedding, jointing, faults, and folds, and

the overall performance was good. In particular, the thickness of the Zhidan group sandstone was 200~300 m, forming a unique ultrathick and weak cementation overburdens in this area. This special geological condition may be one of the main reasons for the significant decrease of the surface subsidence coefficient.

Thus, this paper took Yingpanhao Coal Mine as a geological prototype, through physical and numerical simulation, and deeply studied the movement rule of ultrathick and weak cementation overburdens caused by deep mining and revealed its failure mechanism.

3. Judging Key Stratum

To prove the guess in section 2, this paper used key stratum theory [19] to judge the kinematic property of some strata in the weak cementation overburden. In the following, the criterion on load and stiffness criterion were used to judge their kinematic property.

3.1. Criterion on Load. Assume that the bottom stratum was the key strata in n group strata. Then, the overburden deforms synchronously with it. Considering the principle of curvature equality in synchronous deformation, the load on the bottom stratum can be expressed as

$$(q_n)_1 = \frac{E_1 h_1^3 \sum_{i=1}^{n} \gamma_i h_i}{\sum_{i=1}^{n} E_i h_i^3}, \tag{1}$$

where E is elastic modulus of the strata, h is strata thickness, and γ is unit weight of the strata.

Relative to the bottom stratum, the criterion of the nth stratum to be the key stratum is as follows:

$$(q_n)_1 < (q_1)_1. \tag{2}$$

The criterion of the nth stratum to be the key stratum is as follows:

$$(q_n)_1 < (q_{n-1})_1. \tag{3}$$

Namely,

$$\sum_{i=1}^{n-1} E_i h_i^3 \sum_{i=1}^{n} \gamma_i h_i^3 < \sum_{i=1}^{n} E_i h_i^3 \sum_{i=1}^{n-1} \gamma_i h_i^3. \tag{4}$$

3.2. Stiffness Criterion. Assume that the bottom stratum was the key strata in n group strata. Its limit span must be larger than other strata. Only if this condition is satisfied, can it bear the load from the overburden. Thus, the stiffness criterion of the bottom stratum to be the key stratum is as follows:

$$l_1 = \max\{l_1, l_2, \ldots, l_n\}, \tag{5}$$

where l is limited span of the strata.

The stiffness criterion of the nth stratum to be the key stratum is as follows:

$$l_{n-1} = \max\{l_1, l_2, \ldots, l_n\}. \tag{6}$$

In the following, we take the working face 2201 of mining area 22 in Yingpanhao Coal Mine as the study area. The strata and some parameters are detailed in Table 3.

Firstly, assume that sandy mudstone 2 was the key stratum. Then, equations (7)~(14) can be obtained:

$$(q_1)_1 = \gamma_1 h_1 = 0.81\left(\frac{\mathrm{MN}}{\mathrm{m}^2}\right), \tag{7}$$

$$(q_2)_1 = \frac{E_1 h_1^3 (\gamma_1 h_1 + \gamma_2 h_2)}{E_1 h_1^3 + E_2 h_2^3} = 1.04\left(\frac{\mathrm{MN}}{\mathrm{m}^2}\right), \tag{8}$$

$$(q_3)_1 = \frac{E_1 h_1^3 (\gamma_1 h_1 + \gamma_2 h_2 + \gamma_3 h_3)}{E_1 h_1^3 + E_2 h_2^3 + E_3 h_3^3} = 1.19\left(\frac{\mathrm{MN}}{\mathrm{m}^2}\right), \tag{9}$$

$$(q_4)_1 = \frac{E_1 h_1^3 (\gamma_1 h_1 + \gamma_2 h_2 + \gamma_3 h_3 + \gamma_4 h_4)}{E_1 h_1^3 + E_2 h_2^3 + E_3 h_3^3 + E_4 h_4^3} = 0.10\left(\frac{\mathrm{MN}}{\mathrm{m}^2}\right), \tag{10}$$

$$l_1 = h_1 \sqrt{\frac{2\sigma_1}{(q_1)_1}} = 100.73\ \mathrm{m}, \tag{11}$$

$$l_2 = h_2 \sqrt{\frac{2\sigma_2}{(q_2)_1}} = 27.79\ \mathrm{m}, \tag{12}$$

$$l_3 = h_3 \sqrt{\frac{2\sigma_3}{(q_3)_1}} = 54.65\ \mathrm{m}, \tag{13}$$

$$l_4 = h_4 \sqrt{\frac{2\sigma_4}{(q_4)_1}} = 950.71\ \mathrm{m}. \tag{14}$$

Contrast equations (7)~(14); then, we obtain

$$(q_4)_1 < (q_1)_1 < (q_2)_1 < (q_3)_1, \tag{15}$$

$$l_4 > l_1 > l_3 > l_2. \tag{16}$$

Based on equations (15) and (16), relative to sandy mudstone 2, the Zhiluo formation sandstone is the key stratum.

Then, assume that the Zhiluo formation sandstone was the key stratum. Then, equations (17)~(28) can be obtained:

$$(q_1)_4 = \gamma_4 h_4 = 2.90\left(\frac{\mathrm{MN}}{\mathrm{m}^2}\right), \tag{17}$$

$$(q_2)_4 = \frac{E_4 h_4^3 (\gamma_4 h_4 + \gamma_5 h_5)}{E_4 h_4^3 + E_5 h_5^3} = 3.77\left(\frac{\mathrm{MN}}{\mathrm{m}^2}\right), \tag{18}$$

$$(q_3)_4 = \frac{E_4 h_4^3 (\gamma_4 h_4 + \gamma_5 h_5 + \gamma_6 h_6)}{E_4 h_4^3 + E_5 h_5^3 + E_6 h_6^3} = 4.44\left(\frac{\mathrm{MN}}{\mathrm{m}^2}\right), \tag{19}$$

$$(q_4)_4 = \frac{E_4 h_4^3 (\gamma_4 h_4 + \gamma_5 h_5 + \gamma_6 h_6 + \gamma_7 h_7)}{E_4 h_4^3 + E_5 h_5^3 + E_6 h_6^3 + E_7 h_7^3} = 4.89\left(\frac{\mathrm{MN}}{\mathrm{m}^2}\right), \tag{20}$$

Table 3: Weak cementation strata and some parameters.

No.	Strata	Thickness (m)	Density (kg/m^3)
11	Topsoil	86	1984
10	Sandy mudstone 5	27	2118
9	Zhidan group sandstone	300	2118
8	Coarse sandstone	14	2350
7	Sandy mudstone 4	22	2467
6	Anding formation sandstone	40	2274
5	Anding-Zhiluo formation sandstone	50	2376
4	Zhiluo formation sandstone	120	2418
3	Sandy mudstone 3	23	2405
2	Medium sandstone 1	10	2490
1	Sandy mudstone 2	33	2453

$$(q_5)_4 = \frac{E_4h_4^3(\gamma_4h_4 + \gamma_5h_5 + \gamma_6h_6 + \gamma_7h_7 + \gamma_8h_8)}{E_4h_4^3 + E_5h_5^3 + E_6h_6^3 + E_7h_7^3 + E_8h_8^3} = 5.17\left(\frac{\text{MN}}{\text{m}^2}\right), \tag{21}$$

$$(q_6)_4 = \frac{E_4h_4^3(\gamma_4h_4 + \gamma_5h_5 + \gamma_6h_6 + \gamma_7h_7 + \gamma_8h_8 + \gamma_9h_9)}{E_4h_4^3 + E_5h_5^3 + E_6h_6^3 + E_7h_7^3 + E_8h_8^3 + E_9h_9^3} = 1.73\left(\frac{\text{MN}}{\text{m}^2}\right), \tag{22}$$

$$l_4 = h_4\sqrt{\frac{2\sigma_4}{(q_1)_4}} = 179.88\ \text{m}, \tag{23}$$

$$l_5 = h_5\sqrt{\frac{2\sigma_5}{(q_2)_4}} = 66.93\ \text{m}, \tag{24}$$

$$l_6 = h_6\sqrt{\frac{2\sigma_6}{(q_3)_4}} = 46.75\ \text{m}, \tag{25}$$

$$l_7 = h_7\sqrt{\frac{2\sigma_7}{(q_4)_4}} = 26.46\ \text{m}, \tag{26}$$

$$l_8 = h_8\sqrt{\frac{2\sigma_8}{(q_5)_4}} = 15.79\ \text{m}, \tag{27}$$

$$l_9 = h_9\sqrt{\frac{2\sigma_9}{(q_6)_4}} = 383.97\ \text{m}. \tag{28}$$

Contrast equations (17)~(28); then, we obtain

$$(q_6)_4 < (q_1)_4 < (q_2)_4 < (q_3)_4 < (q_4)_4 < (q_5)_4, \tag{29}$$

$$l_9 > l_5 > l_6 > l_7 > l_8. \tag{30}$$

Based on equations (29) and (30), relative to the Zhiluo formation sandstone, the Zhidan group sandstone is the key stratum.

After judging the key stratum, we can find that the Zhidan group sandstone and the Zhiluo formation have strong control effect. The Zhidan group sandstone and the Zhiluo formation sandstone are the strong-control and the secondary-control strata, respectively.

4. Similar Material Simulation

Considering similar principles, similar material simulations transformed the mine stratum into a similar material model in a certain proportion and minimized the strata movement process caused by resource mining. This is an important method for studying the strata movement. To guarantee the reliability of the research findings, the geometric similarity ratio cannot be too small. The geometric similarity ratio of this physical experiment was 1 : 400, and the similarity ratio of the unit weight was 1 : 1.6. Because of the large depth of the study area, similar material models cannot be used to simulate surface movement. In this paper, a similar material model was only 350 m above the coal seam. The model only includes the Anding formation sandstone with a thickness of 40 meters, the Anding-Zhiluo formation sandstone with a thickness of 50 meters, and the Zhiluo formation sandstone with a thickness of 120 meters, while the Zhidan group sandstone was not included in the model.

4.1. Determination of Kinetic Similarity Ratio in Similar Material Model. Based on the synthetic histogram of mining area 22, the strata can be simplified. Then, the real mechanical parameters of the corresponding strata were used to calculate the mechanical parameters of the physical simulation experiment in the paper, as shown in Table 4.

After determining the mechanical parameters of each stratum in the similar material model, the mica powder, calcium carbonate, and gypsum were selected as similar materials to produce test pieces (Figure 2(a)–2(c)). After the specimen was dried, a compression test can be performed (Figure 2(d)–2(f)). From the results of the compression test, the final ratio of the aggregate and the binder for similar material model can be ensured, as shown in Table 5.

4.2. Design of Similar Material Model Experiment. In order to fully destroy the ultrathick and weak cementation overburden, four working faces named as 2201, 2202, 2203, and 2204 were mined in this paper. The working face was 300 m in width; the coal pillars between the adjacent working faces

Table 4: Comparison table of material mechanical properties.

Strata	Prototype				Model			
	h (m)	H (m)	γ (kN/m^3)	σ (MPa)	h (m)	H (m)	c	σ (MPa)
Coarse sandstone	14		24	24.7	35	15	0.63	0.0386
Sandy mudstone 4	22		25.12	32.93	55	15	0.6	0.0492
Anding formation sandstone	40		22.72	27.42	100	15	0.66	0.0453
Anding-Zhiluo formation sandstone	50		24.05	30.15	125	15	0.62	0.047
Zhiluo formation sandstone	120		24.57	32.43	300	15	0.61	0.0495
Sandy mudstone 3	23		24.64	30.29	57.5	15	0.61	0.0461
Medium sandstone 1	10		22.72	31.43	25	15	0.66	0.0519
Sandy mudstone 2	33		24.81	38.33	82.5	15	0.6	0.0579
Coal	6		12.67	11.44	15	15	1.18	0.0339
Sandy mudstone 1	32		24.09	41.45	80	15	0.62	0.0645

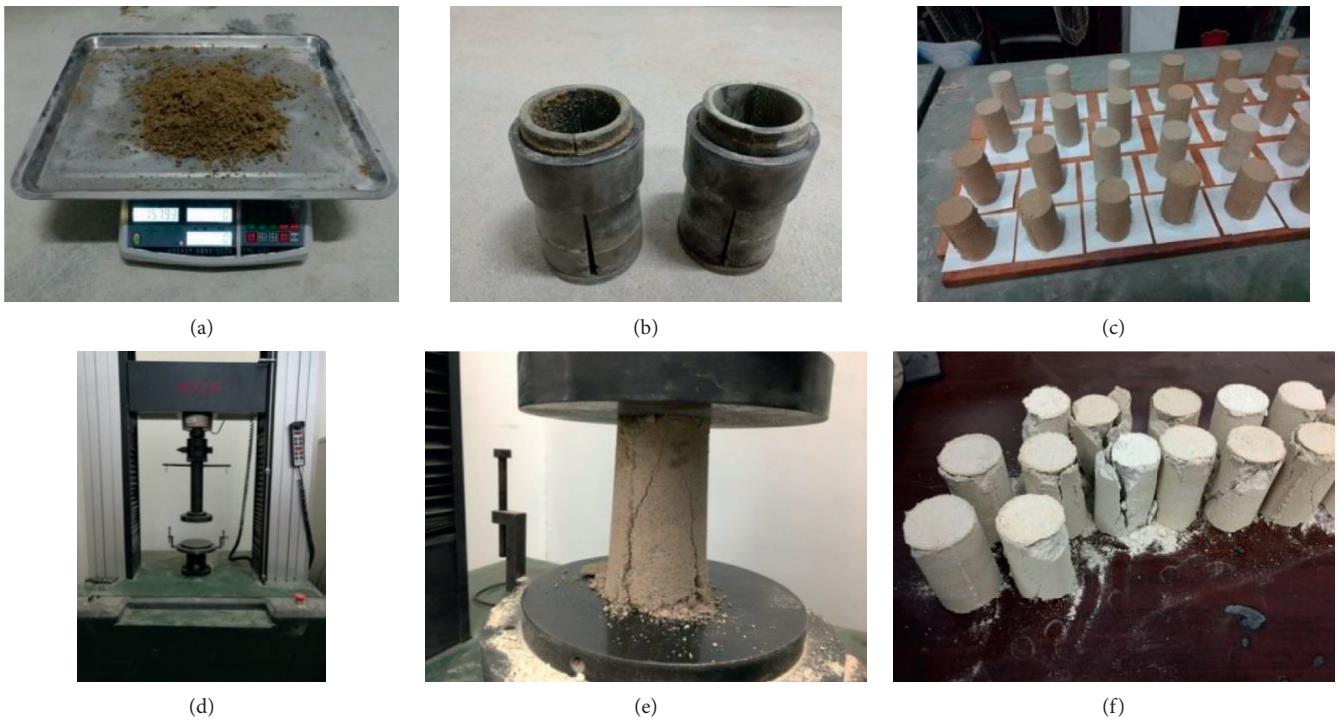

Figure 2: Test pieces production and compression test.

Table 5: Proportion of the similar simulated material.

Strata	Proportion (Sand : micas : cement)	Cement (Gypsum : $CaCO_3$)	Saw dust	Water (%)
Coarse sandstone	80 : 17 : 3	3 : 7	0	10
Sandy mudstone 4	80 : 18 : 2	5 : 5	0	10
Anding formation sandstone 4	73 : 23 : 4	3 : 7	0	10
Anding-Zhiluo formation sandstone	80 : 18 : 2	5 : 5	0	10
Zhiluo formation sandstone	80 : 18 : 2	5 : 5	0	10
Sandy mudstone 3	73 : 23 : 4	3 : 7	0	10
Medium sandstone 1	80 : 18 : 2	7 : 3	0	10
Sandy mudstone 2	80 : 17 : 3	5 : 5	0	10
Coal	80 : 17 : 3	3 : 7	0	10
Sandy mudstone 1	73 : 23 : 4	5 : 5	0	10

were 20 m in width. Due to the wide mining range, we selected a large-scale similar material test bed, which was 5 m long and 0.3 m wide. The load of the unsimulated stratum was equivalent to a uniform load of 15 kPa on top of the model. This paper planned to simulate the uniform load by loading iron blocks, and it was necessary to lay three layers of iron blocks; each of them was a 10 kg cuboid (20 cm in length, 10 cm in width, and 10 cm in height). The strata

design of a similar material model is shown in Figure 3. To simulate the good integrity of ultrathick and weak cementation overburden without large-scale bedding and joint development, no mica flakes were added inside the rock layer as joint surface during the laying the model, and only mica flakes were added as a bedding surface between the two different rock layers.

In a similar material model, a total of 10 observation lines were arranged, as shown in Figure 4. Considering the control effect of the Zhidan group sandstone, when mining the first working face and the second working face, only a uniform load of 5 KPa (equivalent to one layer of iron) was loaded on the top of the model. When the third working face was mined, a uniform load of 10 KPa (equivalent to two layers of iron) was loaded on top of the model. When mining the fourth working face, the top of the model will bear a uniform load of 15 KPa (equivalent to three layers of iron). During the mining process, each excavation was 15 cm (equivalent to 60 m in the field), and the model was monitored before each excavation. The monitoring methods were detailed in Section 4.3. During the excavation process, the movement, damage, slump, and separation of the overburden were recorded in time.

4.3. Similar Material Model Monitoring. In general, the Xi'an Jiaotong University Digital Close-range Industrial Photogrammetry System (XJTUDP) was used to monitor the model during mining. Its measurement accuracy reached 0.064 mm [20]. However, this monitoring method often failed to identify some important points. Thus, this paper also used photographing scale transformation-time baseline parallax (PST-TBP) method to monitor the similar material model to makeup for the lacks of the XJTUDP software. The monitoring schematic diagram was shown in Figure 5, and the parameters of test cameras are shown in Table 6.

The PST-TBP method is detailed as follows [22, 23]. Figure 6(a) shows a schematic diagram of a CCD (Charge Coupled Device) camera capturing images at different photographing distances H3 and H4. In the schematic diagram, the distance between the optical origin (o) and the front end of the camera is H2. D1 on the reference plane and D2 on the object plane are the real-world lengths formed by the view field of the camera at photographing distances H3 and H4, respectively. H1 is the focal length of a camera, N is the maximal pixel number in a horizontal scan line of an image plane, and N is fixed and known as a priori, irrelevant of the photographing distances.

In Figure 6(b), on the object plane, Δx^{de} and Δz^{de} of the corresponding deformation point are

$$\left.\begin{aligned}\Delta x^{de} &= \frac{SA}{Sa}\Delta p_x^{de} = m\cdot\Delta p_x^{de}\\ \Delta z^{de} &= \frac{SA}{Sa}\Delta p_z^{de} = m\cdot\Delta p_z^{de}\end{aligned}\right\}, \tag{31}$$

where m is the photographing scale on the reference plane; Δx^{de} and Δz^{de} are the horizontal and vertical deformation of deformation point on the object plane; and Δp_x^{de} and Δp_z^{de} are the horizontal and vertical parallax of the correspondence image point on the image plane. Note that there exist systematic errors in Δp_x^{de} and Δp_z^{de}.

Δp_x^{de} and Δp_z^{de} can be expressed as

$$\left.\begin{aligned}\Delta p_x^{de} &= \left(x_2^{de} - x_1^{de}\right) - \left(dx_2^{de} - dx_1^{de}\right)\\ \Delta p_z^{de} &= \left(z_2^{de} - z_1^{de}\right) - \left(dz_2^{de} - dz_1^{de}\right)\end{aligned}\right\}, \tag{32}$$

where point a (x_1^{de}, z_1^{de}) and point b (x_2^{de}, z_2^{de}) are the coordinates of the same deformation point on the zero and successive images, respectively. (dx_1^{de}, dz_1^{de}) and (dx_2^{de}, dz_2^{de}) are the systematic errors of the correspondence deformation point on the zero and successive images, respectively. $(\Delta p_x^{de}, \Delta p_z^{de})$ are the parallax of deformation point on the image plane.

To eliminate the digital camera parallaxes caused by camera vibration and the camera stand movement, the control plane, formed by some control points such as the control points C_0-C_7 in Figure 6(b), was used to match a zero image with the successive images, respectively. Note that the control plane near the camera was perpendicular to the photographing direction. The procedure is detailed as follows.

In the control points, equation (32) can be expressed as

$$\left.\begin{aligned}\left(x_2^c - x_1^c\right) - \left(dx_2^c - dx_1^c\right) &= 0\\ \left(z_2^c - z_1^c\right) - \left(dz_2^c - dz_1^c\right) &= 0\end{aligned}\right\}, \tag{33}$$

where (x_1^c, z_1^c) and (x_2^c, z_2^c) are the coordinates of the same control point on the zero successive images, respectively. (dx_1^c, dz_1^c) and (dx_2^c, dz_2^c) are systematic errors of corresponding control point on the zero and successive images, respectively.

Δp_x^c is the parallax in the control point and its equation can be expressed as

$$\left.\begin{aligned}\Delta p_x^c &= \left(x_2^c - x_1^c\right) = \left(dx_2^c - dx_1^c\right) = 0\\ \Delta p_x^{c0} &= \left(-\frac{\Delta Z_S}{Z} - \frac{\Delta f}{f}\right)x_1^c + \Delta k z_1^c + \left(-\frac{f}{Z}\Delta X_S - f\Delta\varphi - \Delta x_0\right) - \frac{x_1^{c2}}{f}\Delta\varphi - \frac{x_1^c z_1^c}{f}\Delta\omega\\ \delta p_x^c &= -\left(\frac{\Delta p_x^c dZ_{S2}}{Z}\right) - \frac{2\Delta p_x^c x_1^c}{f}d\varphi_2 - \frac{\Delta p_x^c z_1^c}{f}d\omega_2 - \frac{\Delta p_z^c x_1^c}{f}d\omega_2 + \Delta p_z^c dk_2 - \frac{df_2}{f}\Delta p_z^c\end{aligned}\right\}, \tag{34}$$

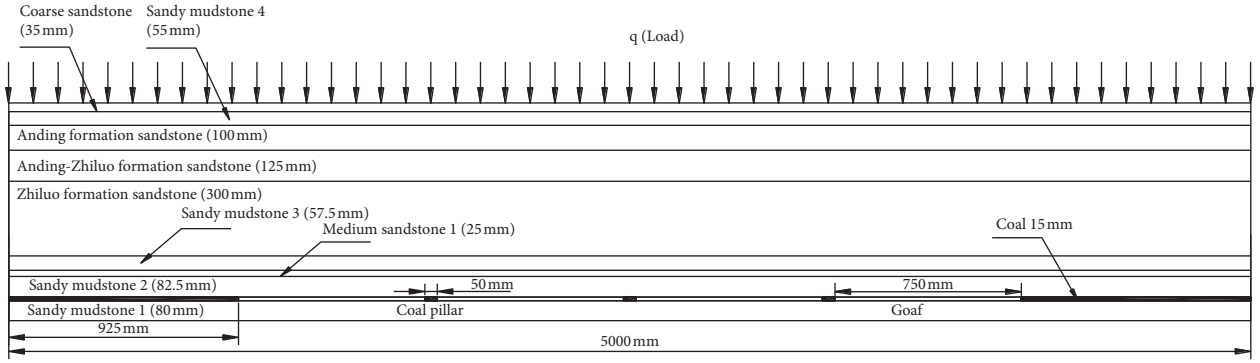

Figure 3: Strata design of the similar material model.

Figure 4: Observation lines on the similar material model.

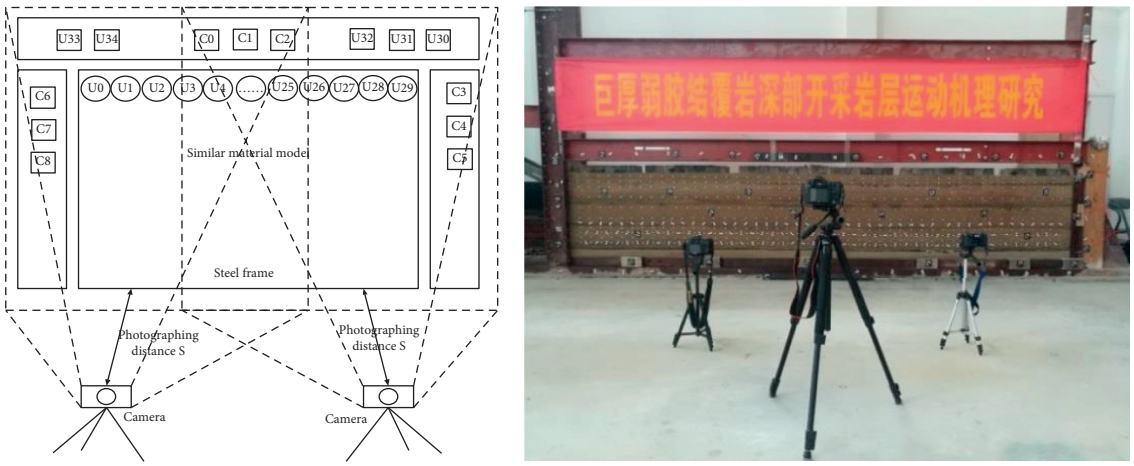

(a) (b)

Figure 5: Field monitoring schematic diagram.

Table 6: Parameters of the Sony-350 camera [21].

Type	Sensor	Sensor scale	Focal length	Active pixels
Sony DSLR A350 (Sony-350)	CCD	23.5 × 15.7 mm	35 mm (27–375)	4592 × 3056 pixels

where (X_S, Z_S, φ, ω, k, f, x_0) are the internal and external orientation elements of the zero and successive images and (ΔX_S, ΔZ_S, $\Delta\varphi$, $\Delta\omega$, Δk, Δf, Δx_0) are the change values of the internal and external orientation elements of the successive image relative to the zero image. $\Delta p^{c0}{}_x$ is the function of the control point coordinates on the image plane, (dZ_{S2}, $d\varphi_2$,

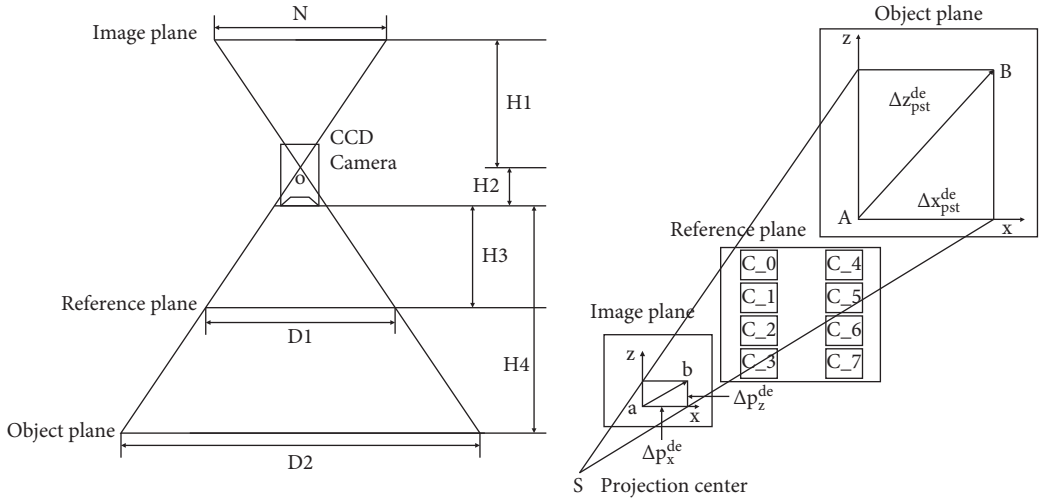

Figure 6: Photographing scale transformation-time baseline parallax method [24].

$d\omega_2$, dk_2, df_2) are the internal and external orientation elements of the successive images themselves, (Δp^c_x , Δp^c_z) are the parallaxes of control points on the image plane, and δp^c_x is the parallax caused by the errors of the internal and external orientation elements of the images themselves and (Δp^c_x , Δp^c_z).

Δp^{c0}_x can also be expressed as

$$\Delta p^{c0}_x = a_x x^c + b_x z^c + c_x + d_x x^{c2} + e_x x^c z^c, \tag{35}$$

where $a_x = -(\Delta Z_S/Z) - (\Delta f/f)$, $b_x = \Delta k$, $c_x = -(f/Z)\Delta X_S - f\Delta\varphi - \Delta x_0$, $d_x = -(\Delta\phi/f)$, (a_x, b_x) and (a_z, b_z) are the parallax coefficients in x- and z-directions, respectively, (c_x, d_x) are the constant parallax coefficients in x- and z-directions, respectively, and (x^c, z^c) are the coordinates of the control points on the image plane.

As $(\Delta p^{c0}_x, \Delta p^{c0}_x)$ are tiny amounts, their quadratic term is negligible and then equation (36) is obtained:

$$\left.\begin{aligned} \Delta p^{c0}_x &= a_x x^c + b_x z^c + c_x \\ \Delta p^{c0}_z &= a_z x^c + b_z z^c + c_z \end{aligned}\right\}. \tag{36}$$

After bary-centralizing the image point coordinates, we get the coordinates $(x^{c'}, z^{c'})$ and the systematic error $(\Delta p^{c0}_x, \Delta p^{c0}_z)$ of the control point in the coordinate system. Equation (37) is obtained when $(\Delta p^{c0'}_x, \Delta p^{c0'}_z)$ only has a random error:

$$\left.\begin{aligned} \Delta p^{c0'}_x &= a_x x^{c'} + b_x z^{c'} \\ \Delta p^{c0'}_z &= a_z x^{c'} + b_z z^{c'} \end{aligned}\right\}. \tag{37}$$

Based on the error equation of (37), we can get the parallax coefficients (a_x, b_x) and (a_z, b_z) of image point in x- and z-directions, respectively. Then, we obtain the systematic errors of deformation points:

$$\left.\begin{aligned} \Delta p^{de0'}_x &= a_x x^{de'} + b_x z^{de'} \\ \Delta p^{de0'}_z &= a_z x^{de'} + b_z z^{de'} \end{aligned}\right\}, \tag{38}$$

where $(x^{de'}, z^{de'})$ and $(\Delta p^{de0'}_x , \Delta p^{de0'}_z)$ are the coordinates and the systematic error of the deformation point in the coordinate system after the bary-centralization, respectively.

Then, the corrected parallax of the corresponding deformation points is obtained:

$$\left.\begin{aligned} \mathrm{cor}\Delta p^{de'}_x &= \Delta p^{de'}_x - \Delta p^{de0'}_x \\ \mathrm{cor}\Delta p^{de'}_z &= \Delta p^{de'}_z - \Delta p^{de0'}_z \end{aligned}\right\}, \tag{39}$$

where $(\mathrm{cor}\Delta p^{de'}_x, \mathrm{cor}\Delta p^{de'}_z)$ are the corrected parallax of deformation points in the coordinate system after the bary-centralization.

Then, we obtain the corrected displacements of deformation points based on the control plane:

$$\left.\begin{aligned} \mathrm{cor}\Delta x^{de} &= m \cdot \mathrm{cor}\Delta p^{de'}_x \\ \mathrm{cor}\Delta z^{de} &= m \cdot \mathrm{cor}\Delta p^{de'}_z \end{aligned}\right\}. \tag{40}$$

where $(\mathrm{cor}\Delta x^{de}, \mathrm{cor}\Delta z^{de})$ are the corrected displacements on the reference plane of deformation points.

According to the photographing scale difference between the control plane and the object plane, we got the actual deformation of the deformation points:

$$\left.\begin{aligned} \Delta x^{de}_{pst} i &= \Delta\mathrm{pstc} \cdot \mathrm{cor}\Delta x^{de} \\ \Delta z^{de}_{pst} i &= \Delta\mathrm{pstc} \cdot \mathrm{cor}\Delta z^{de} \end{aligned}\right\}, \tag{41}$$

where $\Delta x^{de}_{pst} i$ and $\Delta z^{de}_{pst} i$ are the actual spatial deformations on the object plane of deformation, $i = 1, 2, 3 \cdots n$. Δpstc is the coefficient of the photographing scale transformation, and $\Delta\mathrm{pstc} = (H4/H3)$.

5. Analysis of Similar Material Simulation Findings

During the similar material simulation experiment, the movement, damage, slump, and separation of the overburden were recorded in time, and the (XJTUDP) software

and the PST-TBP method were applied to monitor the similar material model of the ultrathick and weak cementation overburden and record its motion regularity.

5.1. Accuracy Assessment of the PST-TBP Method. Since the PST-TBP method is a new monitoring method for monitoring similar material models, it is necessary to evaluate its measurement accuracy. Theoretically, the control point does not move during mining, and its displacement is zero. However, the displacements of these control points obtained by the PST-TBP method were not zero. Therefore, these nonzero displacement values of these control points can reflect the measurement accuracy of the PST-TBP method.

In order to evaluate the measurement accuracy of the PST-TBP method, we selected the control points labelled as R62~R73, and their displacements are described in detail in Table 7. The table indicates that the average error of the right and left cameras is 0.46 mm and 0.48 mm, respectively. Thus, the PST-TBP method can makeup for the deficiencies of the XJTUDP software to some extent.

In addition, we developed manual recognition post-processing software through VC++. Thus, the PST-TBP method can also monitor the deformation of any point on the similar material model and the global dynamic deformation of the similar material model. Furthermore, we applied the PST-TBP method to monitor the dynamic deformation of sluices and bridges, and the test results are reliable. The proposed PST-TBP method overcomes the limitation that the photographing direction in the time baseline parallax method must be perpendicular to the object plane and can monitor the instantaneous dynamic deformation of large-scale structures under unfavorable condition outdoors. Thus, monitoring similar material models is only one of its uses, while the PST-TBP method is of great social benefit and practical value for the safety monitoring and early warning of high-risk structures without manual operation due to environmental hazards.

5.2. Analysis of Failure Characteristics and Movement Rule of the Overburden in the Similar Material Model. After evaluating the measurement accuracy of the PST-TBP method, we further analyzed the experimental results for the movement rules of thick and weak cementation sandstone, while the monitoring data of observation lines I, II, and III were not considered. The following analysis results were attained.

Figures 7(a)–7(c) and 7(e) correspondingly indicate the deformation of the similar material model overburden when the width of working face 2201 was 120 m, 180 m, 240 m, and 300 m, respectively. When the width of working face 2201 was 120 m, the immediate roof suddenly fell down, the height of the roof caving was about 33 m, and the "crescent" type separation extended to 43 m above the coal seam. When the width of the working face 2201 was 180 m, the separation developed to 66 m above the coal seam (the bottom of the Zhiluo formation sandstone). The separation range expanded from 86 m to 120 m, and the separation shape gradually changed from the "crescent" to a "scout" type. When the width of the working face 2201 was 240 m, the separation stopped developing upwards, the separation range continued to expand to 200 m, and the shape of the separation exhibited "boat" type. These indicated that the Zhiluo formation sandstone hindered the upward movement of the separation and played a controlling role. When the width of the working face 2201 was 300 m, the overburden destruction height developed to 112 m above the coal seam, the crack width reached 140 m, and the separation at 43 m above the coal seam became narrower or even closed, and the shape of the separation exhibited "glasses" type. In addition, the maximum size of the broken block was 120 m long and 33 m thick, as shown in Figure 7(a).

The measured data in Yingpanhao Coal Mine gave that the overburden rupture height was about 115 m when the working face 2201 was 300 m in width, and the strike length was about 1800 m. The results of similar material simulation experiments in the paper were consistent with the measured outcomes, indicating that it was reasonable to simulate the control effect of the Zhidan group thick sandstone by reducing the load on the top of the similar material model.

From Figures 7(d) and 7(f), it can be found that when the width of the working face 2201 was 240 m, the Zhiluo formation sandstone was not damaged, but the large simultaneous bending deformation occurred in the Zhiluo formation sandstone and the overburden due to the large range of the goaf. When the width of the working face 2201 was 300 m, the lower part of the Zhiluo formation sandstone was destructed, resulting in the fault-type subsidence of the lower part of the Zhiluo formation sandstone. However, the unbroken parts of the Zhiluo formation sandstone, the Anding-Zhiluo sandstone, and the Anding sandstone can still bear their own weight and the load of the overburden above them, so the top of the model will hardly sink. This phenomenon indicated that the thick sandstone of the Zhiluo formation, the Anding-Zhiluo formation sandstones, and the Anding formation sandstones formed thick Jurassic sandstone formation, which jointly controlled the movement of the overburden.

In Figure 8(a), it is demonstrated that when the width of working surface 2202 was 180 m, the overburden damage height increased to the bottom of the Zhiluo formation sandstone, and the thick sandstone and the overburden above it moved as a whole. However, because of the support of the section coal pillar 1, the movement of the overburden was limited. The observation lines were basically coincident, as shown in Figure 8(b).

Based on Figure 9, it can be concluded that when the width of the 2202 working face was 300 m, slight fractures appeared at 186 m above the coal seam, and the Zhiluo formation sandstone was entirely destroyed. The Anding formation sandstone and the Anding-Zhiluo formation sandstone cannot support the overburden load, generating a large area pressure. The section coal pillar 1 was pressed into the bottom plate, and the overburden continued to move downward.

Table 7: Measurement accuracy (mm).

	Photo no.	DZ62	DZ63	DZ64	DZ65	DZ66	DZ67
Photos from right camera	P1	0.4	−0.23	0.1	−0.42	0.25	−0.88
	P2	−0.6	0.05	−0.2	−0.91	0.2	−0.54
	P3	−0.52	−0.24	0.1	−0.11	0.54	0.24
	P4	−0.57	0.52	0.52	0.85	0.47	0.18
	P5	−0.75	−0.1	0.22	−0.55	0.61	−0.2
	P6	−0.26	−0.35	0.32	−0.07	−0.09	0.7
	P7	−0.2	−0.54	−0.21	−0.09	−0.64	−0.24
	P8	−0.4	−0.29	−0.31	−0.97	−0.26	−0.54
	P9	0.56	0.56	0.31	−0.67	0.13	0.01
	P10	−0.58	−0.38	−0.4	0.85	0.65	0.37
	P11	0.08	0.71	0.13	0.27	0.33	0.52
	P12	−0.49	−0.13	−0.48	0.41	0.88	−0.69
	Accuracy			±0.46			
	Photo no.	DZ68	DZ69	DZ70	DZ71	DZ72	DZ73
Photos from left camera	P13	0.4	−0.3	−0.15	0.26	0.09	−0.15
	P14	0.71	0.47	0.94	0.74	0.22	0.59
	P15	0.29	0.4	0.29	0.63	0.7	0.69
	P16	0.5	0.23	−0.1	0.47	0.78	0.08
	P17	−0.82	−0.54	−0.2	0	−0.34	0.35
	Accuracy			±0.48			

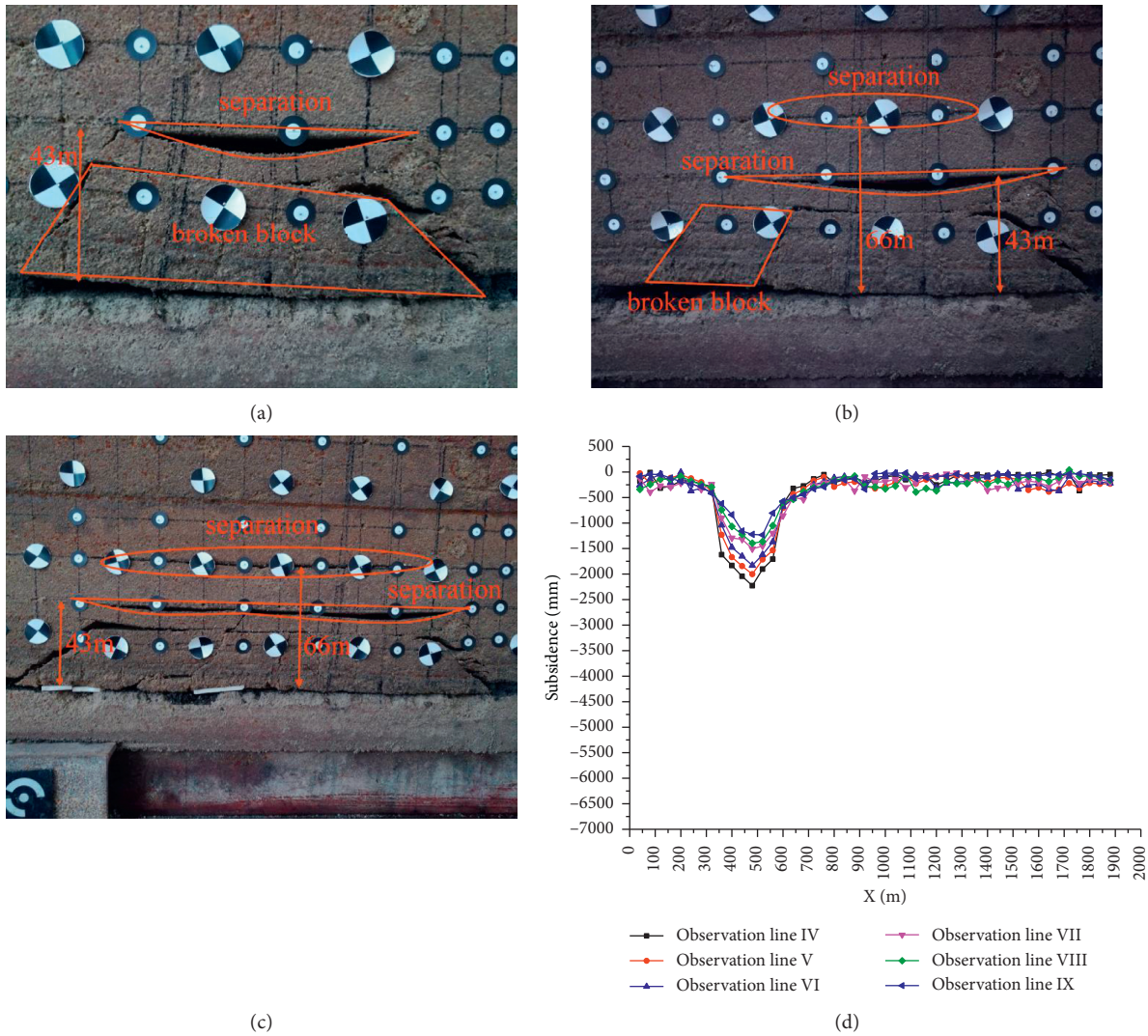

Figure 7: Continued.

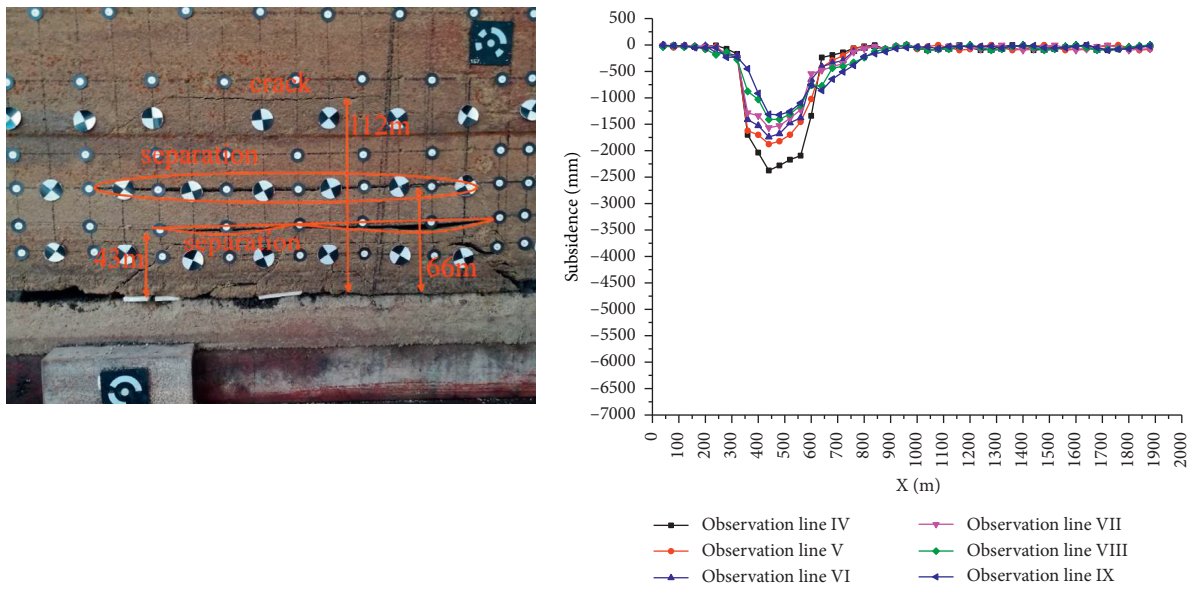

(e) (f)

Figure 7: Failure characteristics and movement rule of the overburden when the working face 2201 was mined. (a) Failure characteristics of the overburden when the working face 2201 was 120 m in width. (b) Failure characteristics of the overburden when the working face 2201 was 180 m in width. (c) Failure characteristics of the overburden when the working face 2201 was 240 m in width. (d) Movement rule of the overburden when the working face 2201 was 240 m in width. (e) Failure characteristics of the overburden when the working face 2201 was 300 m in width. (f) Movement rule of the overburden when the working face 2201 was 300 m in width.

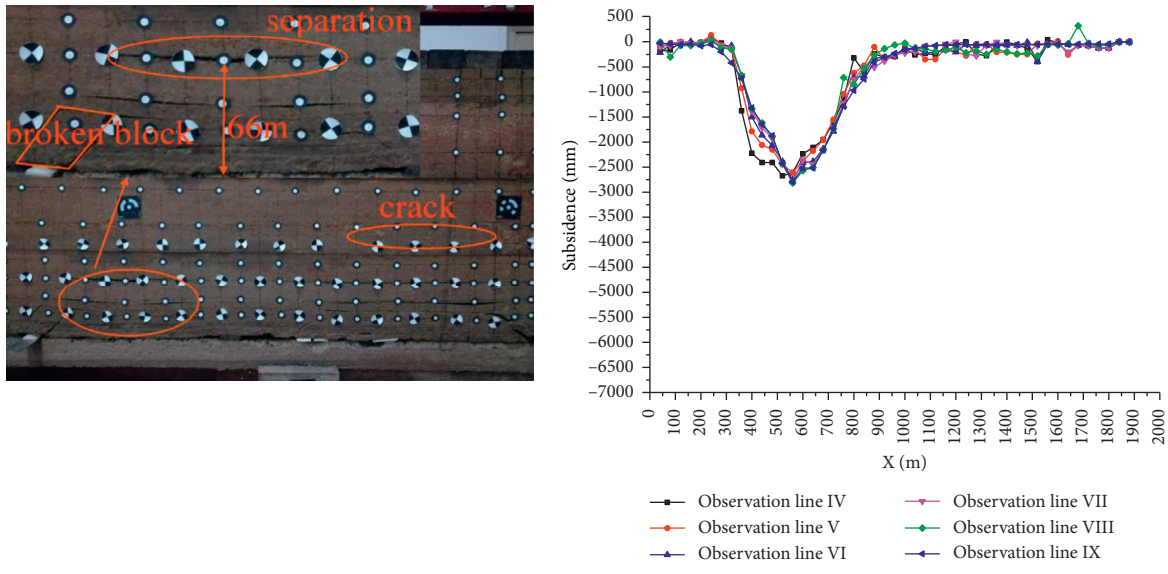

(a) (b)

Figure 8: Failure characteristics and movement rule of the overburden when the working face 2202 was 180 m wide. (a) Failure characteristics of the overburden. (b) Movement rule of the overburden.

It can be seen from Figure 10 that when the working face 2203 owned a width of 300 m, the fractures appeared at 135 m above the coal seam. Because of the large range of the goaf, the Zhidan group sandstone was initially damaged, and the mining pressure was severe. The overburden continued to move downward, leading to the separation under the lower part of the Zhiluo formation sandstone being closed, and the section coal pillar 2 was further pressed into the floor strata with a slight roof cutting phenomenon. Due to the influence of section coal pillar 2, the movement rule of the Zhiluo formation sandstone was wavy.

According to Figure 11, it can be known that when the width of the 2204 working face was 300 m, the failure range

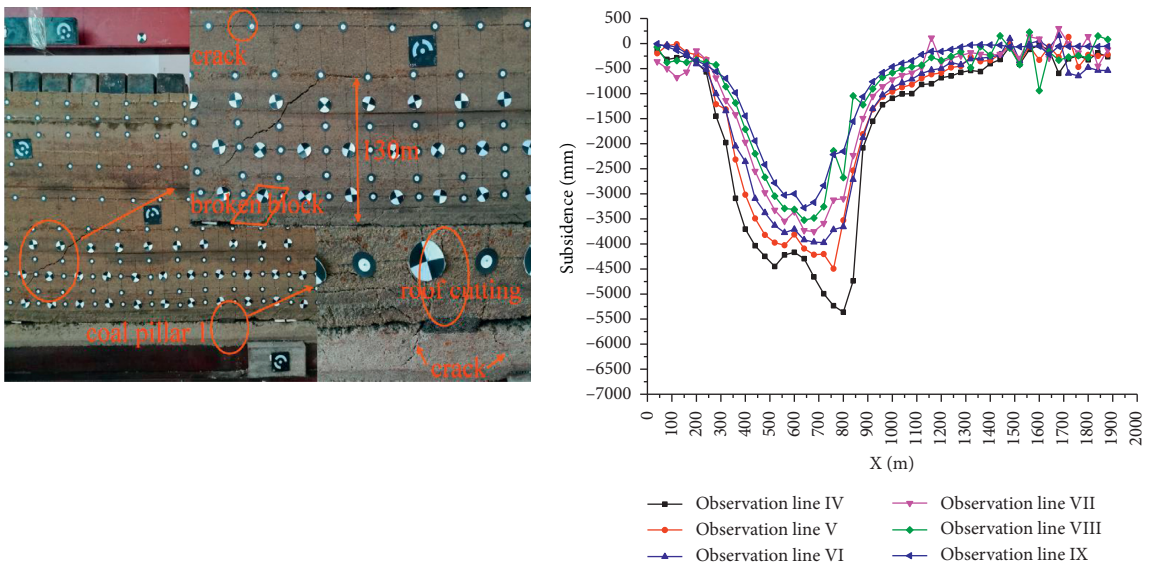

(a) (b)

Figure 9: Failure characteristics and movement rule of the overburden when the working face 2202 was 300 m wide. (a) Failure characteristics of the overburden. (b) Movement rule of the overburden.

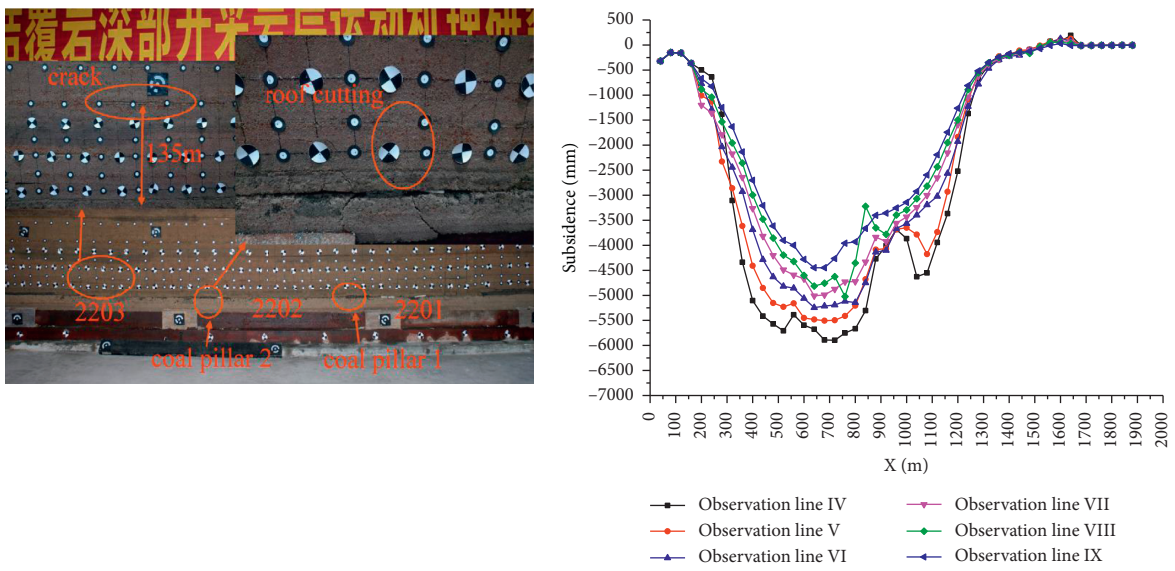

(a) (b)

Figure 10: Failure characteristics and movement rule of the overburden when the working face 2203 was 300 m. (a) Failure characteristics of the overburden. (b) Movement rule of the overburden.

of the overburden is continuously expanding, and the height of the overburden fracture developed to 186 m above the coal seam. Under the influence of repeated mining, the overburden continued to move downward and the movement range kept expanding. With the downward movement of the overburden, the force on the section coal pillar increased, the section coal pillar 3 was pressed into the bottom plate, the bottom below it was pressed out, and the roof cutting phenomenon was severe. Due to the strong supporting effect of the section coal pillar 2, the movement rule of the overburden was "*w*."

5.3. Failure Mode Analysis of Ultrathick and Weak Cementation Overburden

5.3.1. Destruction Rule of Ultrathick and Weak Cementation Overburden. To fully reveal the failure mode of ultrathick and weak cementation overburden, this paper took the working face 2202 as the main research object. In Figure 12, when the working face 2202 had a width of 60 m, no breakage occurred. However, after the coal seam was mined, a pressure release zone was formed above the working face 2202, and the release load was transmitted to both sides of

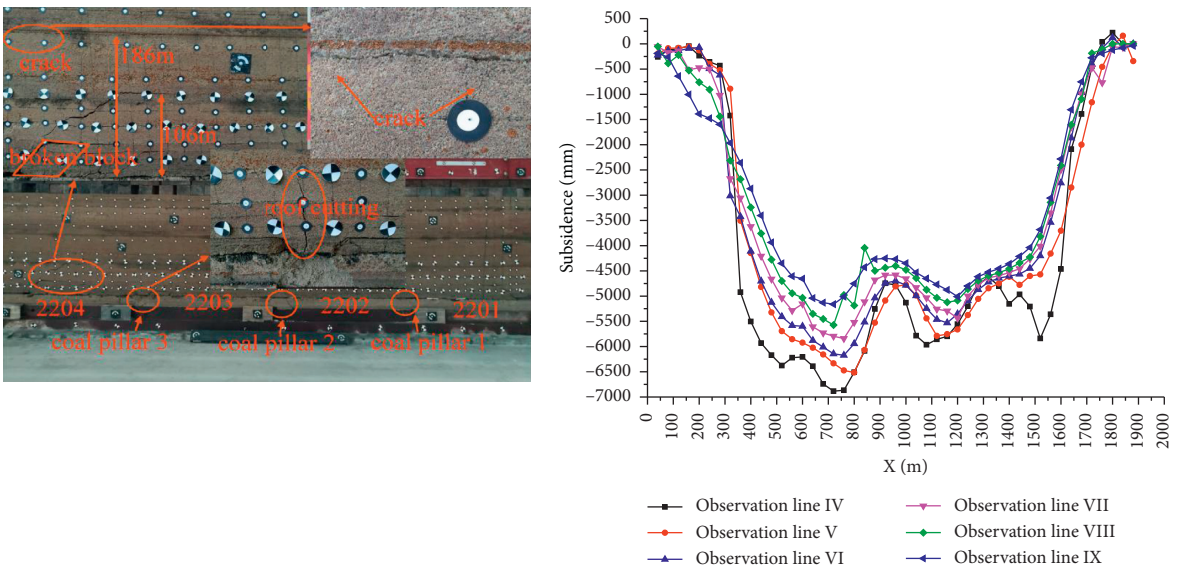

(a) (b)

Figure 11: Failure characteristics and movement rule of the overburden when the working face 2204 was 300 m. (a) Failure characteristics of the overburden. (b) Movement rule of the overburden.

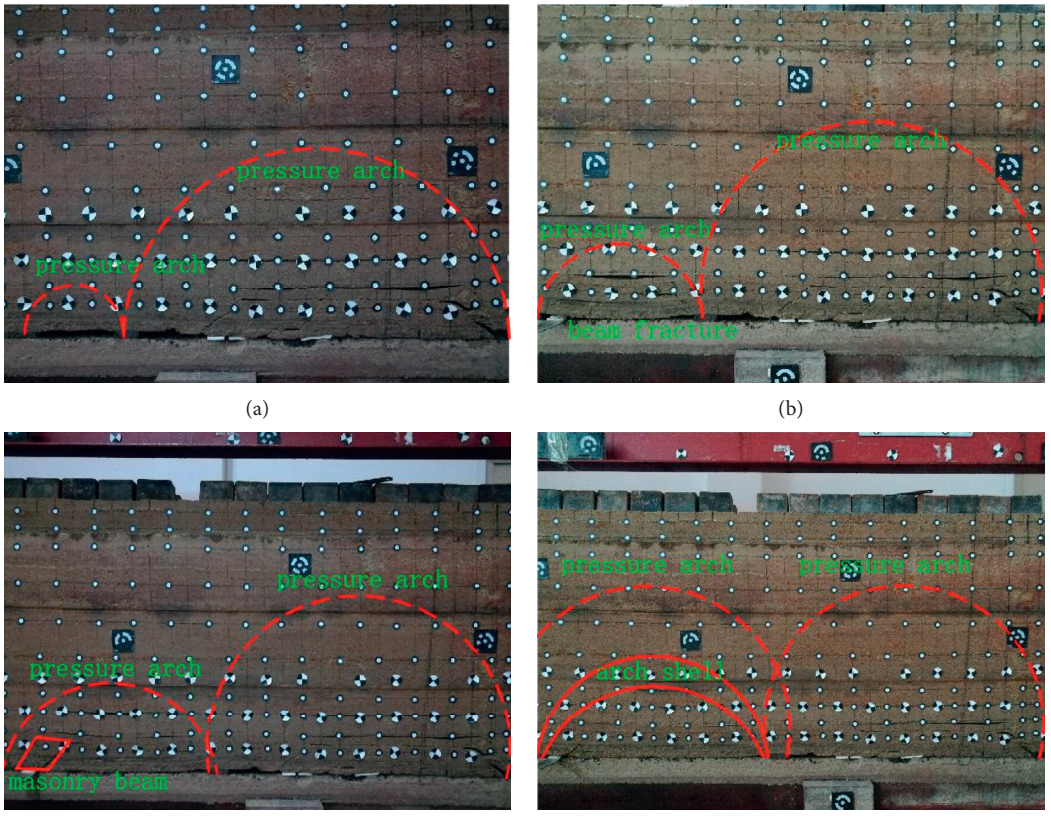

(a) (b)

(c) (d)

Figure 12: Continued.

(e)

Figure 12: Failure mode of ultrathick weak cementation overburdens: (a) the working face 2202 was 60 m in width; (b) the working face 2202 was 120 m in width; (c) the working face 2202 was 180 m in width; (d) the working face 2202 was 240 m in width; (e) the working face 2202 was 300 m in width.

the working face 2202, thereby creating a small pressure arch. At this moment, the height and feet of the pressure arch in the overburden caused by mining the working surface 2201 were substantially unchanged, and a "small-large" camel-peak pressure arch was formed. When the width of the working face 2202 was 120 m, the beam damage occurred on the immediate roof, the height of the pressure arch above the working face 2202 developed upward, and the pressure arch span increased. Next, the height of the pressure arch above the working face 2202 gently developed upward, and the arch feet were substantively unchanged. When the working face 2202 had a width of 180 m, the cyclic fracturing occurred on the immediate roof to attain a masonry beam structure, the pressure arch above the working face 2202 kept developing upward, and the pressure arch span continued to increase. Consequently, the height and feet of the pressure arch caused by mining the 2201 working surface remained almost unmoved. When the width of the working face 2202 was 240 m, there were double-arched cracks above the working face 2202 to build an "arch shell" structure, and the pressure arch above the working face 2202 kept growing upwards, forming a "big-large" camel-peak pressure arch. The pressure arch formed by the two mined working faces generated a stress concentration zone above the section coal pillar and pressed the section coal pillar into the bottom plate. When the working face 2202 possessed a width of 300 m, the double-arched cracks developed forward to acquire a "semi-arched" structure. Simultaneously, the upper part of the camel-peak pressure arch communicated to form a single-peak large pressure arch. From the findings of the physical simulation, the failure mode of the ultrathick and weak cementation overburden was composed of the "beam" failure on the thin weak cementation sandstone and the "arch shell" type failure on the thick weak cementation sandstone, forming a "beam-arch shell" combination failure mode.

5.3.2. Stress Analysis on the Beam-Arch Shell Combination Failure Mode of Ultrathick and Weak Cementation Overburden. In the early mining, the beam bending deformation occurred on the immediate roof (thin weak cementation sandstone) because of the small mining range. When the first mining face was mined, the immediate roof can be regarded as a fixed beam. When the adjacent working face was mined, the immediate roof can be considered as a simply supported beam. The simplified mechanical model of the immediate roof can be seen in Figure 13.

In Figure 13, the D section is an arbitrary section of the beam, and point A is an arbitrary point on section D. The tensile stress and shear stress at point A are correspondingly as follows:

$$\left.\begin{aligned} \sigma &= \frac{12M_D y}{h^3} \\ \tau_{xy} &= \frac{3}{2}Q_D h\left(\frac{h^2-4y^2}{h^3}\right) \end{aligned}\right\}, \tag{42}$$

where σ is the normal stress at point A, τ_{xy} is the shear stress at point A, M_D is the bending moment at section D, Q_D is the shear force at section D, y is the distance from point A to the neutral axis of the rock beam, and h is the thickness of the rock beam.

Based on the material mechanics, the expressions of M_D and Q_D are shown as follows:

$$\left.\begin{aligned} M_D &= \frac{q}{12}\left(12Lx_d - 6x_d^2 - 4L^2\right) \\ Q_D &= qL\left(1-\frac{x_d}{L}\right) \end{aligned}\right\}, \tag{43}$$

where q is the overburden load, $2L$ is the span of the rock beam, and x_d is the distance along the x-direction from the origin of coordinate system to section D.

Substituting formula (43) into formula (42), the tensile stress and shear stress at point A are attained:

$$\left.\begin{aligned} \sigma &= \frac{q\left(12Lx - 6x^2 - 4L^2\right)y}{h^3} \\ \tau_{xy} &= \frac{3}{2}qLh\left(1-\frac{x}{L}\right)\left(\frac{h^2-4y^2}{h^3}\right) \end{aligned}\right\}. \tag{44}$$

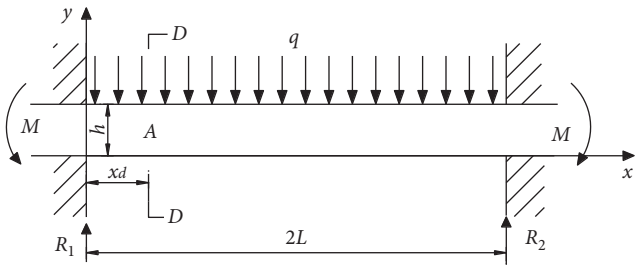

Figure 13: Stress analysis of rock beam at arbitrary point.

The immediate roof of the first mining working face can be regarded as a fixed beam. The maximum tensile stress and the maximum shear stress arose at both ends of the suspended strata. When the tensile stress or shear stress reached the ultimate tensile strength or the ultimate shear resistance strength, tensile or shear failure happened at this moment. The immediate roof of adjacent working faces can be taken as simply supported beams. The maximum shear stress appeared at both ends of the suspended strata, and the maximum tensile stress occurred in the middle position. When the tensile stress in the middle position of the rock beam reached the ultimate tensile strength first, the tensile failure befalled in the middle position of the rock beam. When the shear stress at the two ends of the rock beam first attained its ultimate shear strength, the shear failure happened at both ends of the rock beam. In Figure 7(a), the immediate roof of the first mining working face can be seen as a fixed rock beam and its failure location was at the ends of the immediate roof. In Figure 12(b), the immediate roof of the working face 2202 can be considered as a simply supported rock beam, and the intermediate position of the immediate roof was the first to cause tensile failure.

The "arch shell" failure of ultrathick weak cementation overburden was actually the phenomenon that the strata damaged when the pressure arch of the ultrathick weak cementation overburden achieved the limit. Thus, this paper applied the pressure arch theory to analyze the "arch-shell" type damage of ultrathick weak cementation overburden. The mechanical model of the pressure arch is shown in Figure 14.

In Figure 14(a), the pressure arch owned the strong compression resistance, but its bending resistance was poor, and the load q_0 on the vault was transmitted to the arch feet. The load on the vault included the self-weight of the overburden above the arch and the additional load from the topsoil. q_1 and q_2 were the side loads caused by the disturbance stress and the original strata stress field. The C section was the vault section, T_C was the vault horizontal thrust, and F_A and F_B are the supporting forces of the arch feet. Since the overburden stress was not uniform, the paper regarded the side load as a uniform load q_c for the convenience of calculations.

In Figure 14(b), assuming that the pressure arch model is a parabola, the pressure arch parabolic equation can be expressed as

$$y = -mx^2 + nx + d. \tag{45}$$

The coordinates of arch foot A(0, 0), arch foot B(2l, 0), and vault C(l, h) can be substituted into equation (45):

$$y = -\frac{h}{l^2}x^2 + \frac{2h}{l}x, \tag{46}$$

where $2l$ represents the pressure arch span and h gives the pressure arch height.

Equation (47) can be attained from the force balance and moment balance conditions at points A, B, and C:

$$\left.\begin{aligned} &F_A \cdot 2l + q_c \cdot \frac{h^2}{2} - \frac{q_0 \cdot (2l)^2}{2} - \frac{q_c \cdot h^2}{2} = 0 \\ &-F_B \cdot 2l - q_c \cdot \frac{h^2}{2} + \frac{q_0 \cdot (2l)^2}{2} + \frac{q_c \cdot h^2}{2} = 0 \\ &\frac{F_A \cdot 2l}{2} - T_A \cdot h - \frac{q_c \cdot h^2}{2} - \frac{q_0 \cdot 2l}{2} \cdot \frac{2l}{4} = 0 \\ &T_A + q_c \cdot h - T_B - q_c \cdot h = 0 \end{aligned}\right\}. \tag{47}$$

From the computation, the reaction forces in the horizontal and vertical directions of the arch feet follow:

$$\left.\begin{aligned} &T_A = T_B = \frac{q_0 l^2}{2h} - \frac{q_c h}{2} \\ &F_A = F_B = q_0 l \end{aligned}\right\}. \tag{48}$$

From the calculation outcomes of the pressure arch reaction force, the bending moment, shear force, and axial force balance equation of the arbitrary section of the arch tracing line are sequentially determined, and the bending moment, shear force, and axial force in the section are obtained. In Figure 15(a), section D of the arch tracing line has an angle of α with the horizontal direction, and the bending moment, shear force, and axial force balance equation of section D are correspondingly

$$\left.\begin{aligned} &M_D = F_A x_d - T_A y_d - \frac{q_0 x_d^2}{2} - \frac{q_c y_d^2}{2} \\ &Q_D = (F_A - q_0 x_d)\cos\alpha - (T_A + q_c y_d)\sin\alpha \\ &F_{ND} = (F_A - q_0 x_d)\sin\alpha + (T_A + q_c y_d)\cos\alpha \end{aligned}\right\}, \tag{49}$$

where M_D is bending moment of section D, Q_D is the shearing force of section D, and F_{ND} is the axial force of section D.

Substituting formula (48) into formula (49), the internal force analytical solution in section D can be obtained:

$$\left.\begin{aligned} &M_D = q_0 x_d\left(l - \frac{x_d}{2}\right) - \left(\frac{q_0 l^2}{2h} - \frac{q_c h}{2} + \frac{q_c y_d}{2}\right) y_d \\ &Q_D = -q_0 \cos\alpha x_d - q_c \sin\alpha y_d + q_0 l \cos\alpha - \left(\frac{q_0 l^2}{2h} - \frac{q_c h}{2}\right)\sin\alpha \\ &F_{ND} = -q_0 \sin\alpha x_d + q_c \cos\alpha y_d + q_0 l \sin\alpha - \left(\frac{q_0 l^2}{2h} - \frac{q_c h}{2}\right)\cos\alpha \end{aligned}\right\}. \tag{50}$$

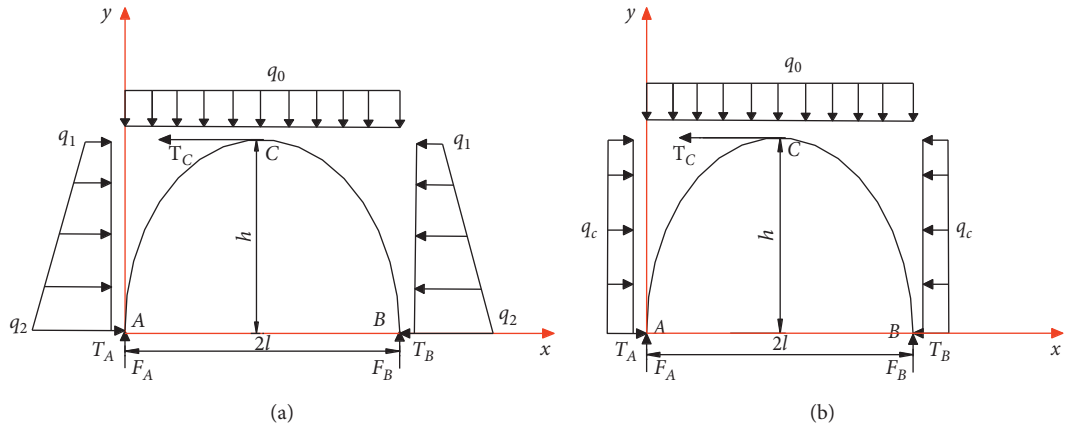

Figure 14: Stress diagram of pressure arch.

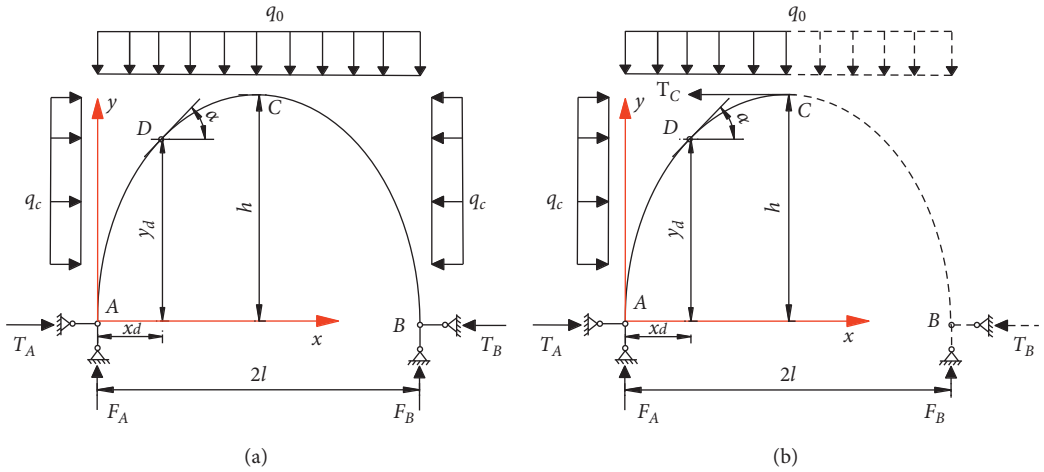

Figure 15: (a) Stress analysis on arbitrary section of complete pressure arch. (b) Stress analysis on arbitrary section of semipressure arch.

In the early mining, the span of the pressure arch above the goaf gradually increased with the width of the working face, and the height of the pressure arch gradually developed upwards. When the stress in the pressure arch reached the sandstone ultimate strength, the overburden would be destroyed and the cracks would occur. It can be seen from the literature that the failure modes of pressure arch included four modes of compression failure, tensile failure, shear failure, and composite failure [25]. The "arch-shell" failure in Figure 12(d) was caused by the pressure on the vault reaching the ultimate strength of the ultrathick weak cementation overburdens, which was a compression failure. When the mining range reached a certain level, the height of the fractured arch no longer continued to develop upward and the fractured arch continued to go forward as the mining range kept expanding. Then, the overburden was destroyed in the form of a half arch. From our analysis, the semiarch mechanical model was similar to the full arch pressure mechanics model, so its failure mode was consistent with the complete pressure arch. In Figure 15(b), the bending moment, shearing force, and axial force of the arbitrary section D of the half arch are the same as equation (6). The "semi-arch-shell" structure in Figure 12(e) was pressure shear damage, because the arch waist position bears the vertical downward load of the overburden and upward sloping forces of the lower strata and reached the shear ultimate strength of ultrathick and weak cementation overburden.

6. Numerical Simulation

To offset the insufficiency of similar material simulation method in studying the bottom-up evolution of space-time in deep mining strata movement, UDEC6.0 discrete element simulation software was used for auxiliary research. Based on the synthetic histogram of mining area 22 of Yingpanyu Coal Mine, an initial two-dimensional numerical model was constructed with the length of 3000 m and the height of 763 m. The grid size varied slightly along the height of the strata. The constitutive model was the Moor Coulomb model, and the selection of the strata mechanical parameters in the model was based on indoor measured rock mechanics parameters. The bottom boundary of the model was a vertical displacement constraint boundary, the top was a free

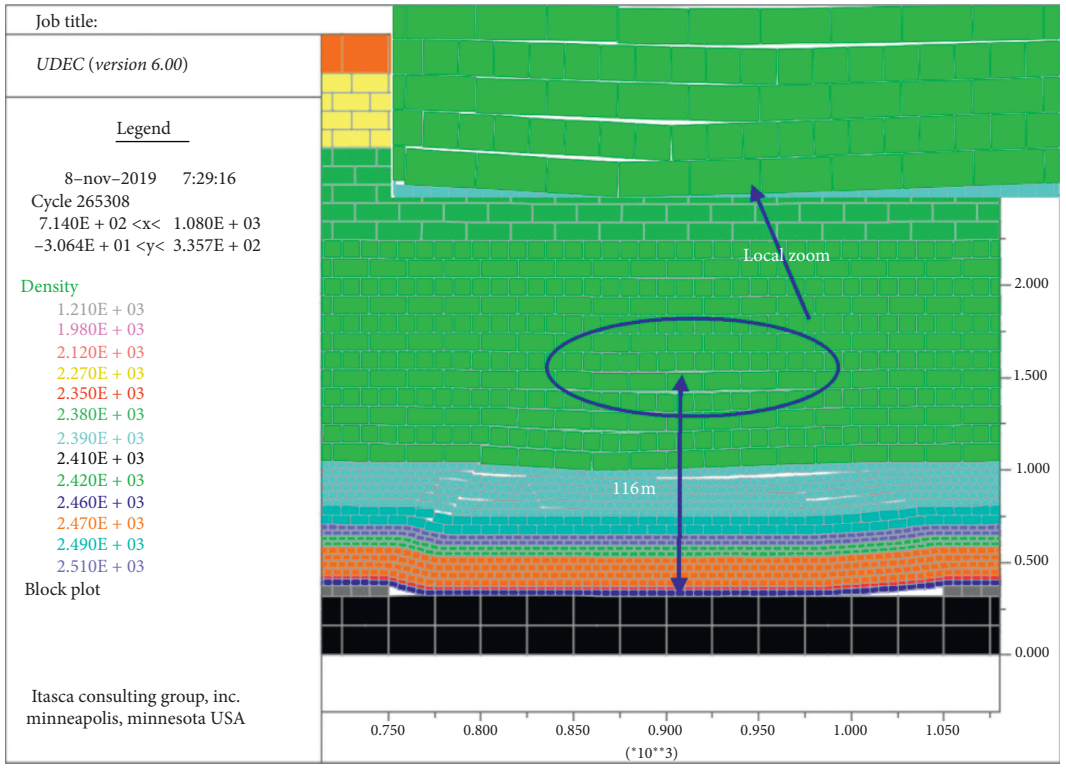

Figure 16: Failure characteristics of the overburden in mining single working face.

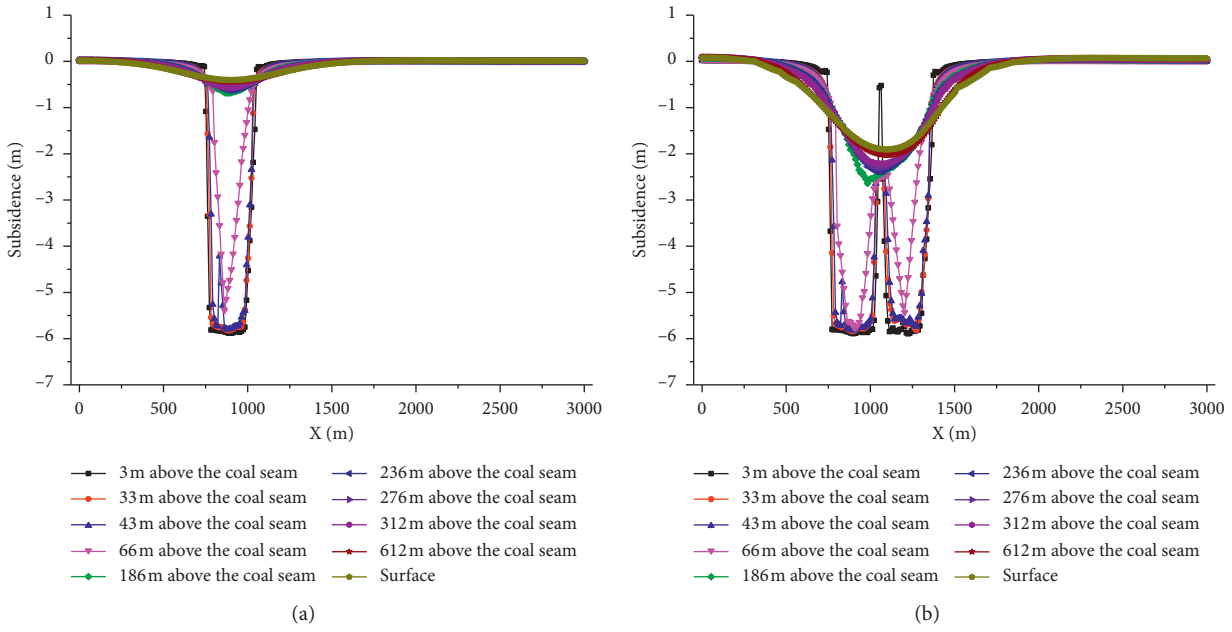

Figure 17: Continued.

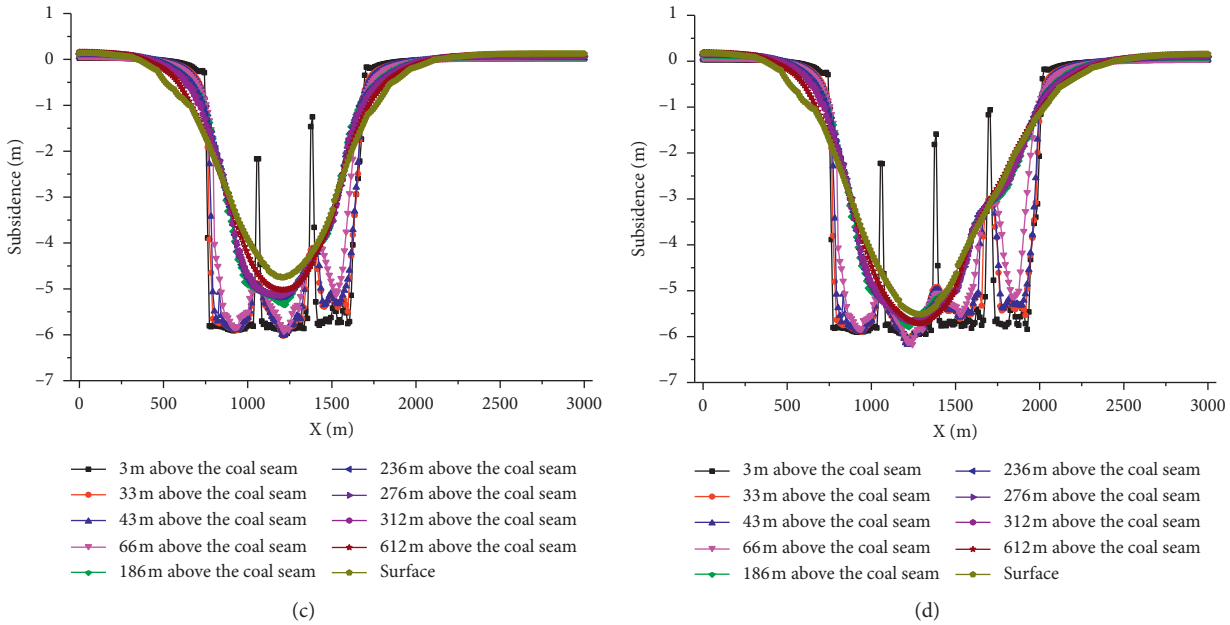

Figure 17: Subsidence of multiworking faces mining in different depth: (a) single mined working face; (b) two mined working faces; (c) three mined working faces; (d) four mined working faces.

boundary, and the left and right boundaries were the horizontal displacement constraint boundaries.

It can be seen from Figure 16 that when the width of the working face was 300 m, the height of the water suture zone was about 116 m, which was only 1 m different from the measured value of 115 m. The maximum surface subsidence was 407 mm, which was only 59 mm away from the measured value of 348 mm. This suggested that the numerical model established in the paper was reasonable and can be regarded as a virtual similar material model.

From Figure 17, it can be found that when the first working face was mined, the surface subsidence value was 407 mm. For this moment, the Zhidan group sandstone and Jurassic sandstone formations had certain control functions and coregulated the surface deformation. When the second working face was mined, the surface subsidence value was 1907 mm, and the Jurassic sandstone formations were entirely destroyed with losing the bearing capacity. However, the sandstone of the Zhidan group was not completely damaged and can still effectively delimit the surface deformation. When mining the third working face, the sandstone of the Zhidan group was fractured for the first time, and the surface sunk in a fracture manner. The maximum subsidence value of the surface reached 4752 mm. When the fourth working face was mined, the overburden was continuously wrecked and the surface subsidence value attained 5516 mm. The surface still has not been fully mined and more mining space is required to extend full mining degree.

Meanwhile, the numerical simulation also demonstrated to a certain extent that it was feasible to simulate the control effect of the Zhidan group sandstone by altering the weight of the iron on the top of the model during mining.

7. Conclusion

In this work, via field investigations, we analyzed the reasons for the small surface subsidence of deep mining with ultrathick and weak cementation overburden. The similar material and numerical simulations were employed to study the strata movement rule of ultrathick and weak cementation overburden. In addition, we applied photographing scale transformation-time baseline parallax (PST-TBP) method to monitor similar material model to compensate for the deficiencies of the digital close-range industrial photogrammetry system (XJTUDP) software. The following findings were obtained:

(1) The PST-TBP method can makeup for the deficiency of the XJTUDP software to a certain extent. In similar material model monitoring, the average errors of the right and left cameras were 0.46 mm and 0.48 mm, respectively. Thus, we can use the PST-TBP method to manually measure the important points that cannot be automatically identified by the XJTUDP software.

(2) The water suture zone of ultrathick weak cementation overburdens was significantly larger than that of the medium-hard and weak overburden areas in middle-eastern China. Similar simulation outcomes indicated that the height of the caving zone was about 66 m and the height of water suture zone was about 112 m, which was evidently larger than that of the medium-hard and soft overburden in middle-eastern China under the same mining conditions.

(3) It was feasible to simulate the control effect of the ultrathick Zhidan sandstone by altering the weight of iron block on the top of the similar material model.

When the first working face of the similar material model was mined, the height of the water suture zone was about 112 m, which was very close to the corresponding measured value of 115 m. Also, the numerical simulations demonstrated that the downward transfer rule of the load of the Zhidan group sandstone and its overburden was consistent with the load variation on the top of the similar material model in the paper, suggesting the reliability of similar simulation findings.

(4) The first breaking span of the immediate roof reached 120 m, and the cyclic fracturing length was about 60 m. The size of the fracture block was larger (the largest size of the broken block, 120 m long and 33 m thick) than that of the Carboniferous-Permian coal seam in the middle-eastern mining area of China.

(5) There existed separation at 43 m and 66 m above the coal seam. With the increase of mining range, the evolution rule of the separation at 43 m above the coal seam was "crescent" type, "pot" type, "boat" type, and "eye" type. The evolution rule of the separation at 66 m above the coal seam was "dash" type and "crescent" type and finally closed.

(6) The failure mode of the ultrathick and weak cementation overburden was "beam-arch shell" failure, and the failure boundary was arch. The failure mode of thin and weak cementation overburdens was "beam" type failure, and finally the masonry beam structure was formed. The failure mode of thick and weak cementation overburden was "arch-shell" type failure. With the further expansion of the mining area, it gradually altered from a complete "arch-shell" type to "semi-arch-shell" type.

(7) The Zhidan group sandstone was the chief control structure, and the Jurassic sandstone rock formation was the secondary control structure, which cooperatively regulated the surface deformation. When the ratio of width to depth was about 1.3, the sandstone of the Zhidan group was destroyed for the first time, and the surface sunk in a fractured manner.

The findings in this paper provide a scientific basis for the precise control design of strata movement of deep mining with the ultrathick and weak cementation overburden. It has great potential applications and scientific significance in green mining, environment-damage control, and scientific mining of deep resources with the ultrathick and weak cementation overburden.

Data Availability

The data used to support the findings of this study are available from the corresponding author upon request.

Conflicts of Interest

The authors declare that there are no conflicts of interest regarding the publication of this paper.

Acknowledgments

The authors gratefully acknowledge the financial support from the National Natural Science Foundation of China (Grant no. 51974292), Postgraduate Research & Practice Innovation Program of Jiangsu Province (Grant no. KYCX19_2162), and Postgraduate Research & Practice Innovation Program of China University of Mining and Technology (Grant no. KYCX19_2162).

References

[1] N. Park, J. Holder, and J. Olson, "Discrete element modeling of fracture toughness tests in weakly cemented sandstone," in *Proceedings of the Gulf Rocks 2004, the 6th North America Rock Mechanics Symposium (NARMS)*, pp. 5–9, Houston, TX, USA, June 2004.

[2] S. Ma and X. B. Wang, "Experimental study on mechanical characters of neogene weak cementation rock," *Yellow River*, vol. 38, pp. 121–124, 2016, in Chinese.

[3] F. Zhou, W. B. Sun, J. L. Sun et al., "Experimental study on nano-silica modified cement base grouting reinforcement materials," *Geomechanics and Engineering*, vol. 20, pp. 67–73, 2020.

[4] Y. Xue, W. Sun, and Q. Wu, "The influence of magmatic rock thickness on fracture and instability law of mining surrounding rock," *Geomechanics and Engineering*, vol. 20, pp. 547–556, 2020.

[5] J. Ju and J. Xu, "Structural characteristics of key strata and strata behaviour of a fully mechanized longwall face with 7.0 m height chocks," *International Journal of Rock Mechanics and Mining Sciences*, vol. 58, pp. 46–54, 2013.

[6] J. Zuo, J. Wang, and Y. Jiang, "Macro/meso failure behavior of surrounding rock in deep roadway and its control technology," *International Journal of Coal Science & Technology*, vol. 6, no. 3, pp. 301–319, 2019.

[7] L. Holla and M. Buizen, "The ground movement, strata fracturing and changes in permeability due to deep longwall mining," *International Journal of Rock Mechanics and Mining Sciences & Geomechanics Abstracts*, vol. 28, no. 2-3, pp. 207–217, 1991.

[8] X. Jialin, L. Guoming, Z. Weibing, and Q. Ming-gao, "Influence of the key strata in deep mining to mining subsidence," *Journal of China Coal Society*, vol. 32, pp. 686–690, 2007, in Chinese.

[9] B. H. Yu, W. B. Zhu, and J. L. Xu, "Numerical simulation of surface subsidence induced by deep mining," *Journl of Mining and Safety Engineering*, vol. 24, pp. 422–426, 2007, in Chinese.

[10] J. Z. Wang and Y. Zhang, "*Study on the Relation of the Mining Degree and the Surface Subsidence Coefficient*", pp. 10–13, Mine Surveying, 1996, in Chinese.

[11] Y. Wang, Z. X. Tan, and P. X. Li, "" Research on the subsidence rule of deep mining in 1-km ming"," *Coal Science and Technology*, vol. 4, pp. 1–4, 2013, in Chinese.

[12] L. H. Sun, "Structural evolution and rock pressure activity regularity of weakly cemented strata of the large mining height work face in western China," *Chinese Journal of Rock Mechanics and Engineering*, vol. 36, p. 1820, 2017, in Chinese.

[13] J. W. Sun, J. G. Liu, D. M. Han, and N. J. Li, "Development height prediction of water-conducting fracture zone of extremely weak cementation overburden in fully mechanized caving," *Mining Surveying*, vol. 2, pp. 19–21, 2012, in Chinese.

[14] W.-X. Li, L. Wen, and X.-M. Liu, "Ground movements caused by deep underground mining in Guan-Zhuang iron mine, Luzhong, China," *International Journal of Applied Earth Observation and Geoinformation*, vol. 12, no. 3, pp. 175–182, 2010.

[15] F. J. Yang, "Actual measurement of overlying strata and surface movement of full-mechanized caving mining under extremely-thick cretaceous sandstone aquifer"" *Coal Mining Technology*, vol. 19, pp. 95–97, 2014, in Chinese.

[16] X. Y. Yu, J. J. Liu, W. B. Guo, and W. Q. Xu, "Surveying of surface movement rule with giant thick cretaceous sandstone"" *Coal Mining Technology*, vol. 14, pp. 15–17, 2016, in Chinese.

[17] B. Wang, *Study on the Strata and Surface Movement Regular of the Weakly Cemented Rock High Intensity Mining*, China University of Ming and Technology, Xuzhou, China, 2017, in Chinese.

[18] Y. K. Lin, *Study on the Surface and Strata Movement Regular of Mining under the Hugely Thick Weak Cemented Sand*, China University of Ming and Technology, 2018, in Chinese.

[19] F. Xiaojun, W. Enyuan, S. Rongxi, W. Mingyao, C. Yu, and C. Xinqi, "The dynamic impact of rock burst induced by the fracture of the thick and hard key stratum," *Procedia Engineering*, vol. 26, pp. 457–465, 2011.

[20] K. Wu, G.-L. Cheng, and D.-W. Zhou, "Experimental research on dynamic movement in strata overlying coal mines using similar material modeling," *Arabian Journal of Geosciences*, vol. 8, no. 9, pp. 6521–6534, 2015.

[21] G. Zhang, G. Guo, L. Li, and C. Yu, "Study on the dynamic properties of a suspended bridge using monocular digital photography to monitor the bridge dynamic deformation," *Journal of Civil Structural Health Monitoring*, vol. 8, no. 4, pp. 555–567, 2018.

[22] G. Zhang, G. Guo, C. Yu, L. Li, S. Hu, and X. Wang, "Monitoring instantaneous dynamic displacements of masonry walls in seismic oscillation outdoors by monocular digital photography," *Mathematical Problems in Engineering*, vol. 2018, pp. 1–15, 2018.

[23] G. Zhang, G. Guo, C. Yu, and L. Li, "Monitoring dynamic global deflection of a bridge by monocular digital photography," *Stavební Obzor - Civil Engineering Journal*, vol. 27, no. 2, pp. 168–182, 2018.

[24] G. Zhang, C. Yu, G. Guo et al., "Monitoring sluice health in vibration by monocular digital photography and a measurement robot," *KSCE Journal of Civil Engineering*, vol. 23, no. 6, pp. 2666–2678, 2019.

[25] S. Wang, N. Li, C. Li, Z. Zou, and X. Chang, "Análisis de inestabilidad del arco de presión en una mina de carbón bajo diferentes ángulos de estratos," *Dyna Ingenieria E Industria*, vol. 90, no. 3, pp. 279–284, 2015.